Green Chemistry

ROYAL SOCIETY OF CHEMISTRY

PAPER

View Article Online
View Journal | View Issue

Cite this: *Green Chem.*, 2024, **26**, 3239

Donor–acceptor sp^2 covalent organic frameworks for photocatalytic H_2O_2 production and tandem bisphenol-A degradation†

Maojun Deng,‡[a] Linyang Wang,‡[a] Zhongliang Wen,[a] Jeet Chakraborty,[a] Jiamin Sun,[a] Guizhen Wang[b] and Pascal Van Der Voort *[a]

Covalent organic frameworks (COFs) emerge as innovative photocatalysts featuring systematically tuned chemical structures, nano-porosity, and photoelectric properties. We have shown in the last years that COFs are excellent photocatalysts and they are able to produce hydrogen peroxide (H_2O_2) from oxygen and water. Despite the recent surge in the photosynthesis of H_2O_2 using COFs, its subsequent application for tandem pollutant remediation as a tangible green alternative to Fenton chemistry has not yet been comprehensively explored. In this study, we synthesized three highly crystalline sp^2 COFs with different donor–acceptor (D–A) strengths, employing triazine units as the electron acceptor moiety. The D–A alignment promotes photogenerated charge separation, augmenting the photocatalytic process, which resulted in the TMT-TT-COF achieving a H_2O_2 production rate of 1952 μmol g^{-1} h^{-1} without any sacrificial agents. The COFs also manifested a rapid photocatalytic degradation of bisphenol A (BPA) from a variety of real-life waterbodies. This study pioneers the *in situ* H_2O_2 production *via* COFs to subsequently generate other reactive oxygen species (ROS) for direct organic pollutant degradation in the visible region.

Received 23rd October 2023,
Accepted 29th January 2024

DOI: 10.1039/d3gc04045c

rsc.li/greenchem

Introduction

The existential impact posed by environmental pollution has been a major concern for researchers in recent decades. One of the pressing environmental challenges is the degradation of persistent organic pollutants, *e.g.*, bisphenol A (BPA), a ubiquitous compound found in various industrial processes, which is associated with adverse health effects.[1] Although certain strategies including adsorption and biodegradation have been proposed to address this challenge, these strategies frequently suffer the generation of secondary pollutants combined with a low degradation efficiency.[2] Advanced oxidation processes (AOPs), *e.g.*, the Fenton process, can efficiently mineralize organic pollutants into CO_2, H_2O, or inorganic ions and have substantiated the instrumental role of hydrogen peroxide (H_2O_2) in this regard. This has gained significant traction as a clean and sustainable approach for producing reactive oxygen species (ROS) like hydroxyl radicals ($^{\bullet}OH$), which play a vital role in pollutant degradation.[3] However, the development of a tandem process tying the generation of H_2O_2 to its subsequent use in pollutant degradation under green and sustainable conditions has seldom been reported.

Conventional techniques like the anthraquinone process,[4] alcohol oxidation route,[5] and electrochemical procedures[6] have found extensive use in industrial H_2O_2 synthesis. Nevertheless, some are waste-intensive, leading to increased production expenditures. To overcome these issues, photocatalysis is a promising strategy due to its ability to efficiently harness (solar) light energy to achieve light-to-chemical energy conversion. The ideal photocatalytic process is proficient, cost-effective, and energy-conserving, requiring only water, oxygen, light, and catalysts.[7] In light of this, there is a significant interest in the exploration of pioneering photocatalytic materials for water treatment and energy conversion. To date, a variety of photocatalysts have emerged, *e.g.*, (1) traditional inorganic semiconductors (such as TiO_2 which displays notable stability but limited use in the visible spectrum due to wide bandgap);[1,8] (2) two-dimensional materials, such as graphene oxide (GO) or GO-based composites, which exhibit remarkable electrical conductivity. Yet, they are limited by the low absorbance of pure GO in the visible light range and the complex synthesis of its composites.[9,10]

Polymer network semiconductors, *e.g.*, graphitic carbon nitride (g-C_3N_4), conjugated microporous polymers, metal–

[a]*COMOC-Center for Ordered Materials, Organometallics and Catalysis, Department of Chemistry, Ghent University, Krijgslaan 281-S3, 9000 Ghent, Belgium. E-mail: Pascal.Vandervoort@ugent.be*
[b]*State Key Laboratory of Marine Resource Utilization in South China Sea School of Material Science and Engineering Hainan University, Haikou, Hainan 570228, P. R. China*

†Electronic supplementary information (ESI) available. See DOI: https://doi.org/10.1039/d3gc04045c

‡These authors contributed equally to this work.

organic frameworks (MOFs), and covalent organic frameworks (COFs) feature advantageous light absorption properties and can render excellent photocatalytic performance through bandgap and band structure modulation.[11–15] Two-dimensional COFs commonly manifest highly π-conjugated organic frameworks composed of light elements (C, O, N, B, *etc.*) interconnected *via* robust covalent linkages.[16,17] The facile separation and migration of photoinduced charge carriers within COF frameworks is another important aspect that benefits photocatalytic processes.[18] The judicious integration of donor (D) and acceptor (A)-type organic moieties into COF structures offers a tool for engineering the bandgap, enabling deliberate tuning of the electronic structure and conductivity of the material.[19] Till now, the majority of the reported D–A COFs have predominantly relied upon imine linkages,[20–23] which are usually accompanied by compromised stability and limited π delocalization.[24] However, these challenges can be resolved through the construction of COFs containing sp^2 C=C bonds. Especially, the sp^2 vinylene-linked COFs demonstrate an extended π-conjugation, distinguished charge carrier mobility, and exceptional chemical robustness even when subjected to severe environmental conditions, substantiating their great potential in practical applications.[23]

Despite the demonstrated excellent efficiency of COFs in H_2O_2 synthesis,[18,25–31] and parallelly in persistent pollutant decontamination,[32] an in-depth exploration of their potential to govern the concomitant degradation of organic pollutants in water *via in situ* photosynthesized H_2O_2-mediated ROS generation remains underexplored. Nevertheless, this undiscovered field is crucial because it expands the research of H_2O_2 applications by avoiding the time and energy-consuming extraction process of H_2O_2.[15] This extraction is still unattractive for photocatalytically produced H_2O_2 as it is generally present in low concentrations (mM). Thus, we built a tandem method that effectively employs H_2O_2 for environmental remediation. Considering the scarcity of research in this area,[33] our work aims to investigate the practical consequences of using COF-generated H_2O_2 for pollutant degradation, so contributing to a better understanding of the real-world uses of COFs in environmental catalysis. Herein, three metal-free vinylene-linked sp^2 COFs with variable D–A strengths (namely TMT-TT-COF, TMT-N-COF, and TMT-BT-COF, see Fig. 1) were

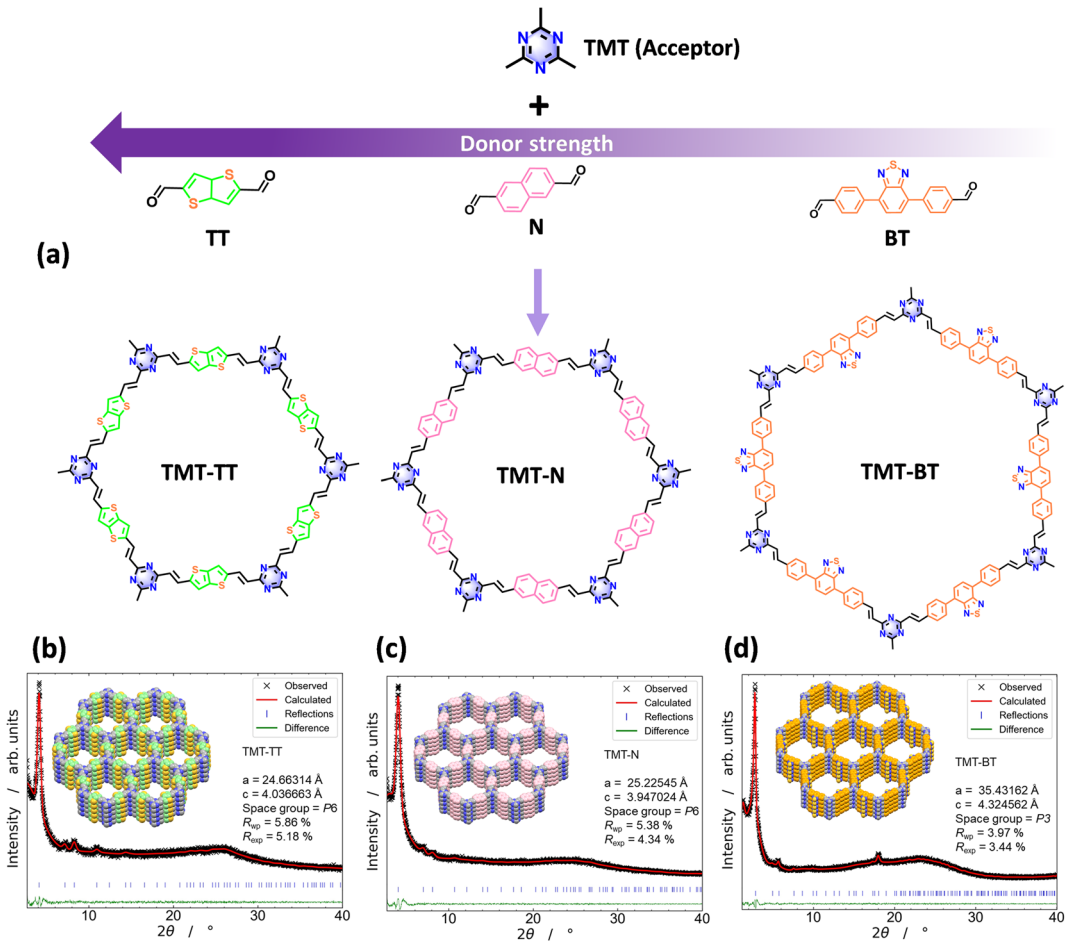

Fig. 1 (a) Synthesis scheme for TMT-TT-COF, TMT-N-COF, and TMT-BT-COF. The PXRD patterns and Pawley refinements of (b) TMT-TT-COF, (c) TMT-N-COF, and (d) TMT-BT-COF.

constructed as photocatalysts to serve this purpose probing simultaneous H_2O_2 production and BPA degradation from water sources. The D–A network allows long-range ordered arrangement and better π–π stacking in these COFs, which led us to analyze the interplay between electronic structures, optical properties, and charge dynamics in these materials. The triazine unit (TMT) and benzothiadiazole moiety (BT) are known as electron acceptors in light of their strong electron affinity.[34,35] Elements including sulfur, on the other hand, are frequently associated with lone pairs of electrons and can act as electron donors. As this implies, thieno[3,2-*b*]thiophene-2,5-dicarboxaldehyde (TT) has a higher donor ability than naphthalene-2,6-dicarbaldehyde (N). Thus, the electron-donating ability is distributed in the following order: TT > N > BT. With this merit, the TMT-TT-COF containing thiophene groups exhibits the strongest D–A characteristics among the three COFs, resulting in a 1952 μmol g^{-1} h^{-1} H_2O_2 generation rate and 96% BPA degradation within 60 min. Additionally, the influencing factors and photocatalytic mechanism of the photocatalytic reaction are discussed in detail.

Results and discussion

The targeted COFs (TMT-TT-COF, TMT-N-COF, and TMT-BT-COF) were synthesized by the Knoevenagel condensation reaction between 2,4,6-trimethyl-1,3,5-triazine (TMT) and aldehyde monomers (TT, N, and BT, respectively) in the solvent mixture of 1,4-dioxane and mesitylene at 150 °C for 72 h (Fig. 1a and Fig. S1, see ESI† for more details). Initially, the crystallinity of the synthesized COFs was revealed by powder X-ray diffraction (PXRD) (Fig. 1b–d). The TMT-TT-COF exhibited a sharp and strong reflection at $2\theta = 4.2°$, which was assigned to the (100) facet. Four more peaks at 7.1°, 8.2°, 10.8°, and 25.2° were attributed to the (110), (200), (210), and (001) facets, respectively. Similarly, an identical PXRD pattern was observed for TMT-N-COF and TMT-BT-COF. Nevertheless, the reflection peak corresponding to the (100) facet of TMT-BT-COF was observed at $2\theta = 2.7°$, which can be attributed to the incorporation of longer linkers. All of the experimental PXRD patterns matched well with the simulated AA-eclipsed layer stacking model with unit cell parameters ($a = b = 24.67$ Å, $c = 4.03$ Å, $\alpha = \beta = 90°$, $\gamma = 120°$ for TMT-TT-COF; $a = b = 25.23$ Å, $c = 3.95$ Å, and $\alpha = \beta = 90°$, $\gamma = 120°$ for TMT-N-COF; and $a = b = 37.62$ Å, $c = 3.76$ Å, $\alpha = \beta = 90°$, and $\gamma = 120°$ for TMT-BT-COF), and the satisfactory agreement factors were found for the TMT-TT-COF (R_{wp} = 5.86% and R_p = 5.12%), TMT-N-COF (R_{wp} = 5.38% and R_p = 4.34%), and TMT-BT-COF (R_{wp} = 3.97% and R_p = 3.44%), respectively. Full profile Pawley refinement of their diffraction patterns revealed a hexagonal structure. Following that, Fourier transform infrared (FT-IR) was utilized to investigate their characteristic bands (Fig. S2†). The disappearance of the carbonyl peaks of the monomers and the appearance of the new C=C stretching vibration peaks at 1613 cm^{-1}, 1624 cm^{-1}, and 1625 cm^{-1} confirmed the conversion of aldehydes to vinylenes in TMT-TT-COF, TMT-N-COF, and TMT-BT-COF, respectively. X-ray photoelectron spectroscopy (XPS) analyses were conducted to further confirm the existing elements of C 1s, N 1s, and S 2p in the TMT-TT-COF (Fig. S3† and Fig. 2). The C 1s spectrum of TMT-TT-COF could be deconvoluted into three peaks at 288.38 eV, 286.63 eV, and 284.5 eV, which can be attributed to "π–π*", "N–C=N", and "C=C/C–C" bonds, respectively. In the N 1s spectrum, the peak located at 399.40 eV is assigned to the triazine moiety. Besides, the peaks observed at 164.02 eV and 165.20 eV in the S 2p spectrum are assigned to the S $2p_{3/2}$ and S $2p_{1/2}$ thiophene monomers, respectively.

Their permanent porosity was accessed by nitrogen sorption measurements at 77 K. In Fig. S4,† both TMT-TT-COF and TMT-N-COF displayed the typical type-I isotherms with a rapid N_2 uptake in the low-pressure region, indicating their microporosity. However, the TMT-BT-COF showed a type-III isotherm with mesoporous characteristics. Additionally, the Brunauer–Emmett–Teller surface area of TMT-TT-COF, TMT-N-COF, and TMT-BT-COF was calculated to be 556 m^2 g^{-1}, 519 m^2 g^{-1}, and 90 m^2 g^{-1}, respectively. The pore size distributions of TMT-TT-COF, TMT-N-COF, and TMT-BT-COF were analyzed by the quenched solid density functional theory (QSDFT) method, yielding estimated values of 1.6, 1.9, and 3.6 nm, respectively, which are closed to the simulated values (Fig. S4†).

From the thermogravimetric analysis (TGA) curves, TMT-TT-COF and TMT-N-COF exhibited better thermal stability than TMT-BT-COF (Fig. S5†). Although all three COFs showed comparable network stability till 350 °C under N_2, TMT-BT-COF experienced more significant mass loss at higher temperatures. This could be explained by the higher conjugation degree of the D–A units introduced in TMT-TT-COF and TMT-N-COF, which increases the thermal stability of COFs whereas the longer linker in TMT-BT-COF weakens it.[24] Afterwards, their morphologies were investigated by field-emission scanning electron microscopy (FE-SEM). In Fig. 2d–f, TMT-N-COF and TMT-BT-COF exhibited spherical nanoparticles with average particle sizes of 3.1 μm and 3.8 μm respectively, while TMT-TT-COF appeared as bipyramidal particles with an average size of 3.25 μm. Transmission electron microscopy (TEM) measurements were employed for further confirmation of the TMT-TT-COF structure (Fig. S6†).

Apart from the investigations of structures and morphologies of these three COFs, their optoelectronic properties are also of crucial significance in photocatalysis. First, diffuse reflectance ultraviolet-visible (UV-vis) spectra were recorded to analyze their optical properties. As Fig. 3a shows, all three COFs displayed broad absorption in the visible-light region, which confirmed their strong visible-light harvesting nature. TMT-N-COF exhibited a maximum absorption peak at 470 nm, which is close to TMT-BT-COF (480 nm). A considerable red-shift to 518 nm was observed for TMT-TT-COF. Using the Tauc plot, the band gaps of TMT-TT-COF, TMT-N-COF, and TMT-BT-COF were calculated to be 1.77 eV, 2.13 eV, and 2.28 eV, respectively (Fig. S7†). On the other hand, the conduction bands (CBs) of TMT-TT-COF, TMT-N-COF, and TMT-BT-COF

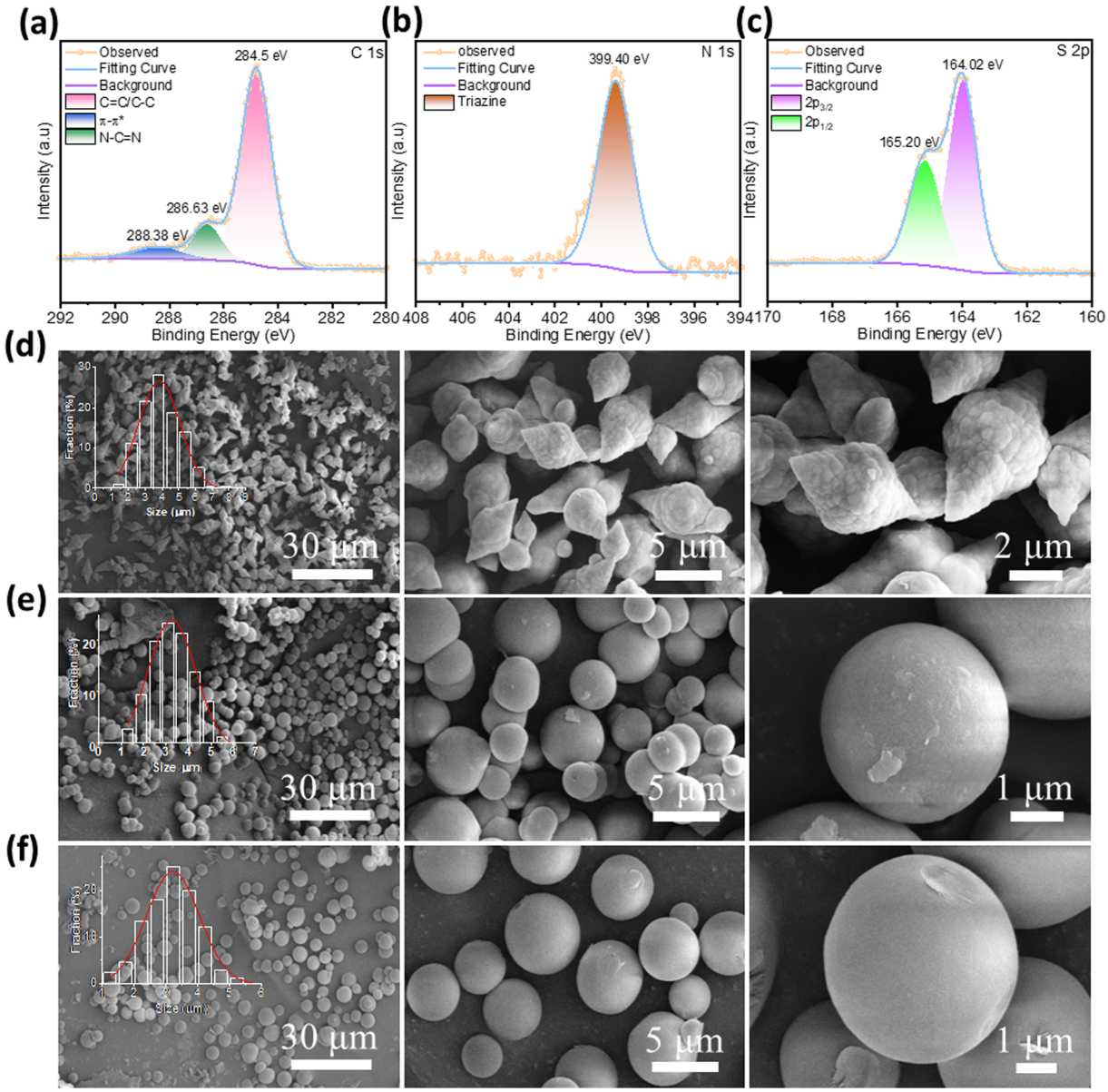

Fig. 2 XPS high-resolution spectra of TMT-TT-COF in the region of (a) C 1s, (b) N 1s, and (c) S 2p. FE-SEM images of (d) TMT-TT-COF, (e) TMT-N-COF, and (f) TMT-BT-COF (inset: the size distribution of the three COFs).

were determined to be −0.46, −0.5, and −0.38 V *vs.* NHE, respectively by Mott–Schottky analysis conducted at their respective isoelectric points (Fig. S8†). Moreover, the positive slopes of the Mott–Schottky analysis suggested that all three COFs are n-type semiconductors, making them good candidates for reduction reactions such as oxygen reduction reaction (ORR) for H_2O_2 production, especially since all the CBM values were more negative than that required for O_2 to superoxide ($O_2/^{\bullet}O_2^-$ = −0.33 V, *vs.* NHE at pH = 7). Accordingly, the valence band maximum (VBM) potentials of TMT-TT-COF, TMT-N-COF, and TMT-BT-COF were measured to be +1.31, +1.63, and +1.9 V *vs.* NHE at pH = 7 (Fig. 3b). Such high VBM values further indicated the suitability of the COFs to oxidize BPA into degradation products (0.77 V, *vs.* NHE at pH = 7).[36]

Furthermore, photoluminescence (PL) spectra were performed to evaluate photoinduced charge separation efficiency. As shown in Fig. S9,† both TMT-BT-COF and TMT-N-COF displayed high PL intensity. It is worth noting that the PL intensity of TMT-TT-COF was significantly weaker than TMT-BT-COF and TMT-N-COF, indicating that TMT-TT-COF had the lowest recombination of charge carriers. To validate the above analysis, transient fluorescence lifetime decay spectra were conducted. By fitting these curves, the average decay lifetimes of 1.77 μs for TMT-TT-COF, 1.38 μs for TMT-N-COF, and 1.37 μs for TMT-BT-COF were obtained in Fig. S10.† The prolonged PL decay lifetime and notably quenched PL emission in TMT-TT-COF, compared to TMT-N-COF and TMT-BT-COF, suggest enhanced charge separation and more

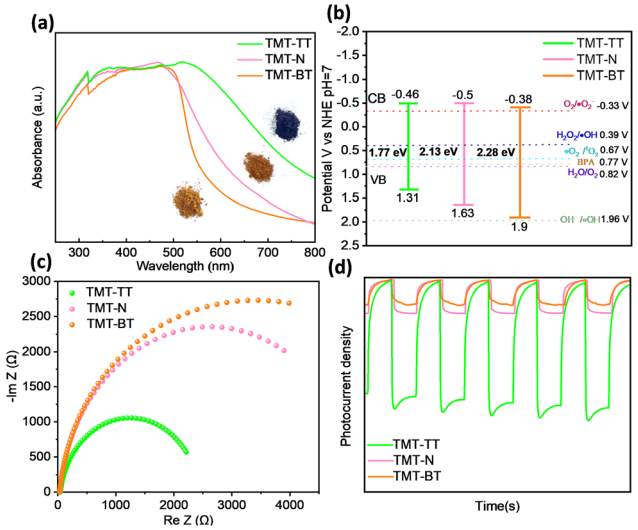

Fig. 3 (a) UV-vis spectra and the color of as-synthesized COFs powder, (b) band alignment, (c) electrochemical impedance spectra (EIS), and (d) photocurrent responses of TMT-TT-COF, TMT-N-COF, and TMT-BT-COF.

extended exciton mobility facilitated by the incorporation of the stronger electron-donating TT moiety into the COF structure.[37–39] Moreover, the electrochemical impedance spectra (EIS) were measured to study the charge transfer resistance. A smaller arc radius for the TMT-TT-COF was observed in the Nyquist plot (Fig. 3c), which illustrates lower charge transfer resistance. After fitting to the Randel circuit, the charge transfer resistance (R_{CT}) values of TMT-TT-COF, TMT-N-COF, and TMT-BT-COF were estimated to be 2067 Ω, 4910 Ω, and 5239 Ω respectively. The photocurrent responses of the COFs were further analyzed to echo the charge transfer trend observed by EIS. As shown in Fig. 3d, TMT-TT-COF possesses the strongest transient photocurrent response, which indicates more efficient charge separation compared to TMT-BT-COF and TMT-N-COF. In general, TMT-TT-COF exhibited better optoelectronic properties than TMT-N-COF owing to the presence of thiophene groups, which resulted in a deeper color of the photocatalytic material (Fig. 3a), enhanced absorption of visible light, a narrower energy band, and higher electron density.

In order to better understand the effect of the building units on the optoelectronic properties of the COFs, their molecular analogues have been theoretically modeled. As shown in Fig. 4, the highest occupied molecular orbital (HOMO) of all three COFs was found to be distributed entirely on these moieties, *i.e.*, on TT, N, and BT units, whereas the lowest unoccupied molecular orbital (LUMO) of TMT-TT-COF and TMT-N-COF were distributed on the whole skeleton, but that of TMT-BT-COF was concentrated only on the BT moiety. This observation highlights the impact of different electron-donating moieties on the electronic distribution of respective COFs. As the TT moiety is highly electron-donating, the triazine unit served as the electron-accepting counterpart in TMT-TT-COF,

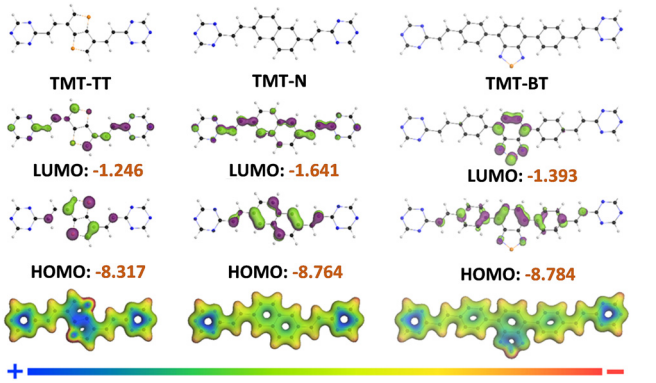

Fig. 4 Distributions of the HOMO and LUMO of TMT-TT-COF, TMT-N-COF, and TMT-BT-COF.

which led to the extended distribution of LUMO over the entire backbone including triazine. A similar situation was encountered for TMT-N-COF as well, despite the relatively suppressed electron-donating ability of naphthalene over TT. BT, on the other hand, is a strong electron-accepting unit, so the LUMO was found concentrated on the BT unit alone. This way, one may retrospect the TMT-BT-COF as more of a heterogeneous molecular analogue of BT, whereas TMT-N-COF and TMT-TT-COF showed extended orbital distributions posing more semiconducting trends. Accordingly, TMT-BT-COF molecular analogue possessed the highest computed bandgap followed by TMT-N-COF and TMT-TT-COF, respectively (Fig. 3b). This order is in line with the experimentally obtained bandgaps of the COFs. The electron densities of the three COFs were also mapped against respective potential energy surfaces. Indeed, as shown in Fig. 4, the sulfur centers in TMT-TT-COF showed the maximum localization of charge density whereas the triazine moiety was the most devoid of it. This demonstrates a relatively heterogenized charge distribution in the material, which is beneficial for its application as a photocatalyst. The extent of such charge density heterogenization was relatively low in TMT-N-COF, and much lower in TMT-BT-COF indicating that these two COFs may perform relatively poorly under photocatalytic conditions when compared to TMT-TT-COF. The experimentally obtained low charge transfer resistance and high photocurrent response of TMT-TT-COF compared to the other two COFs can be justified by this theoretical result as well.

Photocatalytic activity

H_2O_2 production

Given the in-depth evaluation of the physicochemical properties of the COFs highlighting their immense potential to photochemically produce H_2O_2 and degrade BPA, we were inspired to conduct a thorough investigation into both these catalytic aspects. We evaluated their H_2O_2 production efficiency first before probing them into simultaneous BPA degradation by using the *in situ* generated H_2O_2. This

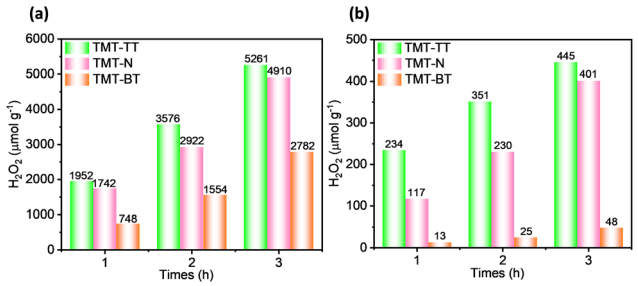

Fig. 5 Photoactivity of the COFs for H_2O_2 production in pure water under the illumination of a 300 W Xe lamp, (a) O_2 atmosphere and (b) Ar atmosphere.

approach allows us to understand the entire breadth of their photocatalytic activity in detail. Initially, the experiments of photosynthesis H_2O_2 were performed under visible light ($420 < \lambda < 700$ nm) irradiation without any sacrificial agents (10 mg of COF in 30 mL Milli-Q water, O_2 or Ar purge 20 min, see ESI† for more details). In the O_2-purged pure water system, the H_2O_2 generation rates for TMT-TT-COF, TMT-N-COF, and TMT-BT-COF were detected to be 1952, 1742, and 748 μmol g^{-1} h^{-1}, respectively (Fig. 5a). When O_2 was replaced by Ar, all the COFs exhibited a considerable reduction in H_2O_2 generation rates, indicating the vital involvement of oxygen in this process (Fig. 5b). Such high H_2O_2 production rates in the O_2 pre-saturated water can be explained by the suitable photochemical properties of the COFs. Moreover, the catalytic activity trend of the three COFs is positively correlated with their corresponding D–A strengths (TMT-TT-COF > TMT-N-COF > TMT-BT-COF). The rational integration of D–A units extended the π-conjugation structure of COFs in x and y plane, leading to high conductivity and efficient electron transport.

Degradation of BPA

Motivated by the H_2O_2 photo-production results, a systematic examination was carried out to assess the practical feasibility of these systems for the photocatalytic degradation of BPA under simulated as well as real-life media. In Fig. 6a, TMT-TT-COF and TMT-N-COF exhibited outstanding BPA degradation efficiency of 96% and 94.7% within 60 min in the Milli-Q water system, respectively. On the contrary, TMT-BT-COF showed relatively low activity with a degradation rate of merely 40%. The kinetic rate constants of BPA photodegradation were evaluated by pseudo-first-order kinetic mode (eqn (S3) and (S4)†). As shown in Fig. S11,† the rate constant of TMT-BT-COF is 0.007, leading to poor performance regarding BPA degradation. In the case of TMT-TT-COF and TMT-N-COF, the rate constants 6.9-fold and 6.4-fold higher than those of TMT-BT-COF were observed, respectively. Similar to the H_2O_2 case, this observation could be ascribed to the incorporation of the D–A building units in TMT-TT-COF and TMT-N-COF, which effectively promotes charge transfer and facilitates charge separation, thereby making them highly efficient on target pollutants. Notably, TMT-TT-COF exhibited decent H_2O_2 production and BPA degradation efficiency compared to similar materials (Tables S2 and S3†). Given its better photocatalytic performance, we utilized TMT-TT-COF as an example to investigate the effect of catalyst dosage on its activity. Accordingly, Fig. 6b illustrates the impact of varying dosages (5 mg, 10 mg, and 15 mg) of TMT-TT-COF on the degradation of BPA over a duration of 60 min. At a dosage of 5 mg, the degradation efficiency of TMT-TT-COF was notably low, reaching only 42%. Conversely, the dosage of 10 mg resulted in a rapid increase in degradation efficiency, achieving 96%. Similarly, a dosage of 15 mg exhibited a faster degradation rate, also reaching 96% after 60 min. These findings highlight the positive correlation between the presence of active substances and the availability of surface-active sites. Considering environmental concerns and consumption reduction, the optimal TMT-TT-COF dosage of 10 mg was employed for subsequent experiments within the following series.

Following establishing the performance of the COFs in Milli-Q water, other types of water and various pHs were also tested. As these real-life conditions can significantly affect the photochemical response of the system, it is imperative to assess their respective impacts on the practical employability of the materials. As shown in Fig. 6c–e, the BPA degradation efficiency of TMT-TT-COF in tap water, lake water, and seawater exhibited a slight decrease compared to its performance in Milli-Q water while remaining at around 80%. The other two materials also manifested a similar decreased catalytic efficiency. Of note, the catalytic activity trend *i.e.*, TMT-TT-COF > TMT-N-COF > TMT-BT-COF, still maintained under these conditions as well. The decreased degradation efficiency in these real-life water systems might be caused by the presence of certain inorganic ions, which can affect the functionality of active sites inside the material.[13] Likewise, diverse chemical conditions in real wastewater may significantly change the pH of the medium too, which can affect the stability and catalytic performance of materials. Thus, the degradation efficiency of TMT-TT-COF toward BPA was evaluated under varying pH values. In Fig. 6f, in the pH range of 3 to 11, TMT-TT-COF showed a favourable performance in the photocatalytic degradation of BPA. Nevertheless, with the increases of alkalinity (pH > 7), its degradation efficiency slightly decreased. This may be explained considering that BPA predominantly exists as negatively charged ions at pH values above 9.6,[2,40] and the zeta potential of TMT-TT-COF becomes more negative as pH rises, leading to the repulsion between the BPA and TMT-TT-COF (Fig. S8a†). Heterogeneous photocatalysis being a surface phenomenon, such electrostatic repulsion diminishes the surface adsorption of BPA and effective charge transfer from COF to the pollutant. Consequently, this repulsive interaction hampers the rate of BPA degradation.[41] On the other hand, even with the inhibition of ROS formation (*e.g.*, $^{\bullet}OH$) under acidic conditions, no significant changes were observed in the degradation of BPA by TMT-TT-COF when compared to neutral

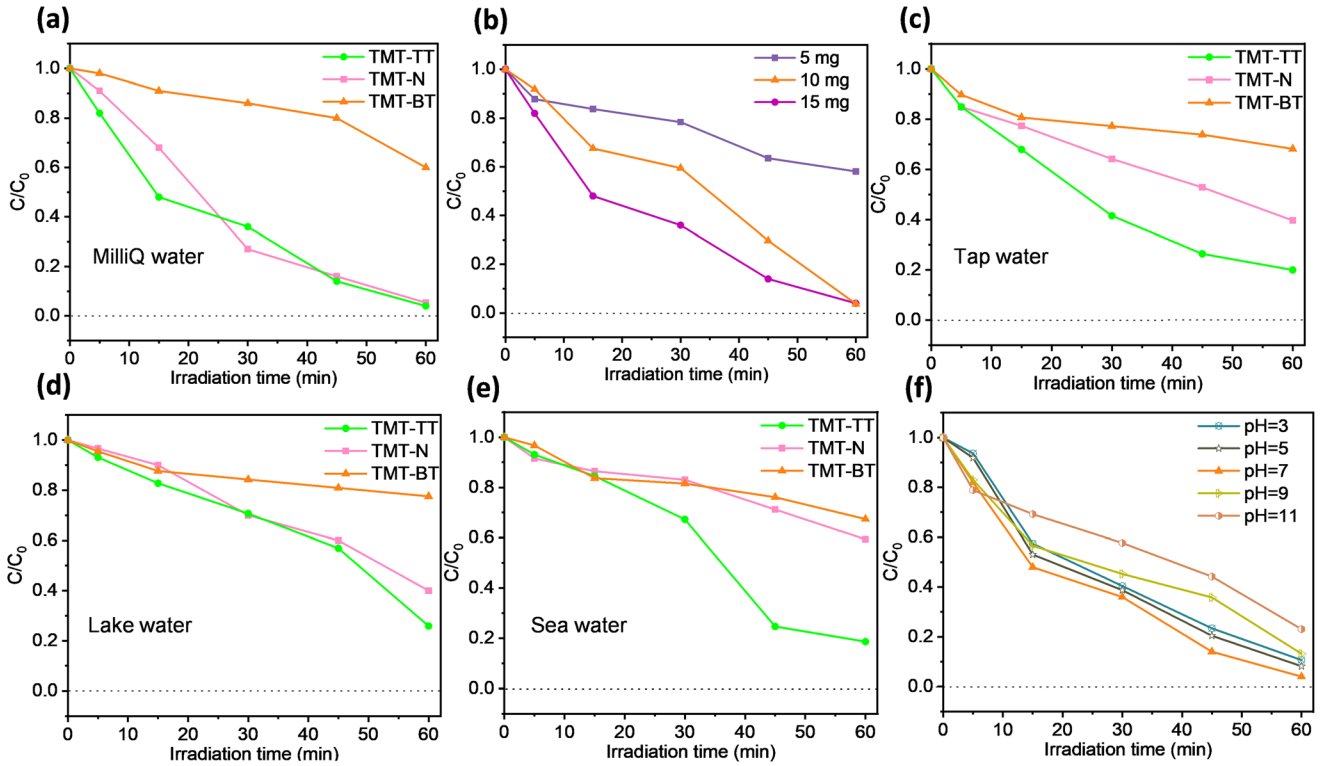

Fig. 6 (a) Photocatalytic performance of TMT-TT-COF, TMT-N-COF, and TMT-BT-COF for BPA photocatalytic degradation, the influence of (b) photocatalyst dosage (TMT-TT-COF), (c)–(e) different water matrix, and (f) the effect of initial pH on the removal rate of BPA with the addition of HCl or NaOH solutions (reaction conditions: BPA = 30 mL of 25 mg L^{-1}, 300 W Xe lamp, C_0 is the absorption of the initial concentration when adsorption–desorption equilibrium is established).

conditions. This can be explained from three aspects: (1) BPA molecules feature two oxygen atoms with negative charges within the hydroxyl groups, along with four negatively charged carbon atoms located *ortho* to the phenolic group. Meanwhile, the TMT-TT-COF is positively charged under acidic conditions (Fig. S8a†), thereby facilitating the interaction between the TMT-TT-COF and BPA molecules;[13,42] (2) COFs may undergo protonation under acidic conditions, thereby enhancing their photocatalytic reaction ability;[42–44] (3) in the context of a photocatalytic system at pH = 3, an increased concentration of H^+ is observed, leading to enhanced H^+ adsorption on the photocatalyst's surface. Consequently, upon contact with the catalyst's surface, O_2 undergoes reduction to form $^{\bullet}O_2^-$ species through the action of photogenerated electrons.[45]

Recyclability, another key indicator regarding practical applications, also needs to be evaluated. For this purpose, the stability of TMT-TT-COF was assessed over five consecutive cycles of photocatalytic degradation targeting BPA. The results revealed that TMT-TT-COF maintained a relatively high level of photocatalytic degradation performance (Fig. 7a). No obvious alterations were observed in the PXRD pattern and FT-IR spectra of the spent TMT-TT-COF (Fig. S12†), implying its excellent stability and recyclability in the degradation of BPA.

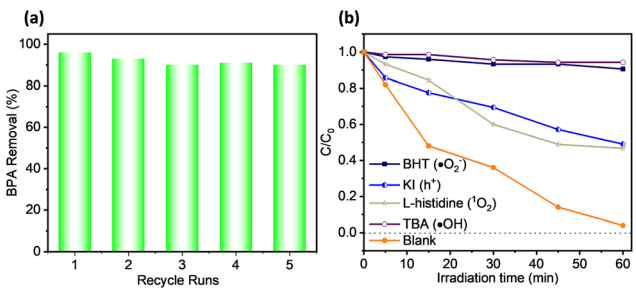

Fig. 7 (a) Recyclability of photocatalytic experiments by TMT-TT-COF. (b) Effects of scavengers (2 mmol L^{-1}) on BPA degradation (reaction conditions: photocatalyst = 10 mg, BPA = 30 mL of 25 mg L^{-1}).

Photocatalytic mechanism analysis and proposed BPA degradation pathways

Considering the remarkable H_2O_2 yield as well as the exceptional degradation performance of BPA demonstrated by TMT-TT-COF, we were intrigued to tie these two catalytic activities together for a thorough understanding of the mechanism. Firstly, we examined H_2O_2 production in an air atmosphere both with and without BPA. H_2O_2 production is

1484 μmol g^{-1} h^{-1} in the absence of BPA, while in the presence of BPA, it decreases to 257 μmol g^{-1} h^{-1}. This phenomenon may imply the role of H_2O_2 in the indirect oxidation of BPA. Subsequently, the free radical trapping experiments were conducted. Butylated hydroxytoluene (BHT), KI, L-histidine, and tertbutyl alcohol (TBA) served as trapping agents for $^{\bullet}O_2^-$, h^+, $^1O_2$, and $^{\bullet}OH$, respectively. Fig. 7b illustrated that the presence of BHT and TBA markedly suppressed the degradation of BPA, suggesting that $^{\bullet}O_2^-$ and $^{\bullet}OH$ radicals serve as crucial active species in the photocatalytic degradation procedure. Moreover, it is observed that both h^+ and $^1O_2$ also exerted a certain inhibitory effect in the BPA degradation process. As all three COFs exhibited varying levels of H_2O_2 production even in the Ar-purged water (Fig. 5b), we reckoned that the oxidation of water to oxygen has taken place at VB of TMT-TT-COF. To prove this, we conducted controlled photoreactions in a N_2 atmosphere, using silver nitrate ($AgNO_3$) as an electron scavenger in deaerated water. Micro-GC measurements confirm the presence of O_2 after 6 hours of irradiation, thereby substantiating the generation of O_2 on the VB of TMT-TT-COF (Fig. S13†). This inspired us to carry out controlled experiments on the photocatalytic degradation of BPA under Ar atmospheres, which also showed a satisfactory degradation efficiency of 64% (Fig. S14†). It's noteworthy that in our photocatalytic system, we found that h^+ can directly oxidize and degrade BPA. To illustrate this, we substituted the aqueous medium with the redox-stable organic solvent acetonitrile (ACN) and introduced an electron scavenger to perform the degradation process under an Ar atmosphere. Fig. S15† shows that h^+ directly accounted for 28% of BPA degradation. As illustrated in the hole-capture experiments conducted with KI (Fig. 7b), the holes present in the COF preferentially oxidize I^- to I_2 rather than oxidizing BPA. However, in this experiment, we also observed *ca.* 50% degradation of BPA within 1 hour. Given the suppression of direct oxidation of BPA, this outcome affirms the involvement of H_2O_2 in the indirect oxidation of BPA, aligning with our initial hypothesis. Based on these results, a plausible mechanism is proposed in Fig. 8. Firstly, under light irradiation, the COF-based photocatalyst was excited to transfer photogenerated electrons from VB to CB. This process induced the migration of photogenerated carriers within the material. In the CB, the accumulated electrons reacted with O_2 to form the $^{\bullet}O_2^-$ radicals. Subsequently, these radicals engage in indirect two-electron ($2e^-$) ORR pathways, leading to the production of H_2O_2. Then the formed H_2O_2 undergoes further reduction, resulting in the generation of $^{\bullet}OH$, which plays the most significant role in BPA degradation. This explanation justifies the corresponding control experiment results with BHT and TBA. Of note, $^{\bullet}OH$ can also be generated by direct water oxidation by h^+. However, the potential requirement for this to happen is significantly higher than the VBM of the material. This substantiated that the reduction of H_2O_2 is the only possible pathway to produce $^{\bullet}OH$ under our catalytic medium. The h^+, on the flip side, effectively oxidize H_2O to O_2 and H^+ species as well as directly oxidize and destroy BPA molecules. At the same time, the $^{\bullet}O_2^-$ obtained in the CB undergoes a subsequent oxidation process, ultimately yielding $^1O_2$.

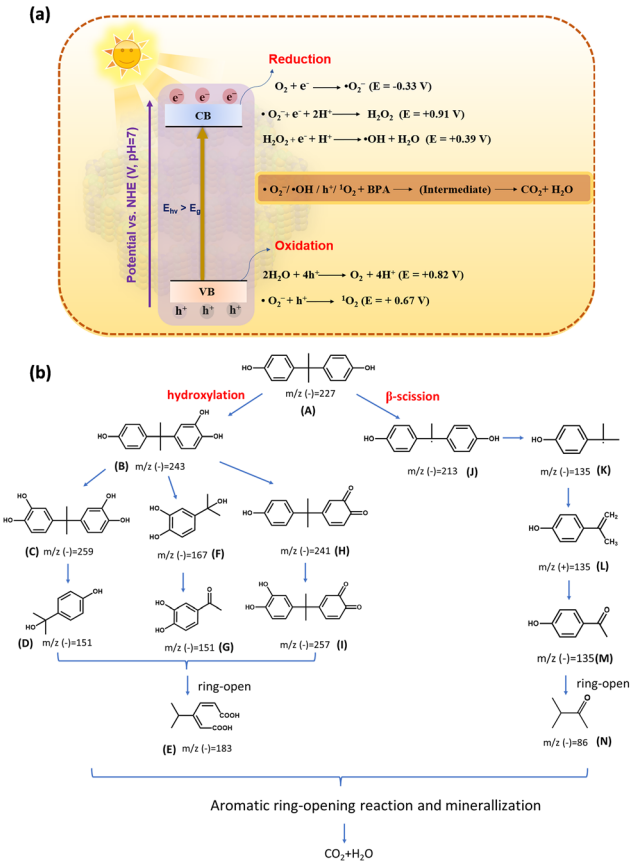

Fig. 8 (a) Proposed mechanism for the photocatalytic degradation of BPA, (b) proposed BPA degradation pathways for TMT-TT-COF.

To gain a comprehensive understanding of the BPA degradation process, liquid chromatography-mass spectrometry (LC-MS) analysis was employed to examine potential intermediate products (Fig. S16†). Based on the results of radical trapping experiments and the identified intermediates, we present potential pathways for the photocatalytic degradation of BPA in Fig. 8b. In our photocatalytic system, hydroxylation and β-scission were observed to be the two main transformation pathways for BPA degradation. It is worth mentioning that the presence of $^{\bullet}O_2^-$ plays a crucial role in this photocatalytic degradation process, as it serves as the precursor for the formation of highly reactive secondary radicals, namely $^{\bullet}OH$ and $^1O_2$. **Pathway I:** initially, BPA is electrophilically attacked by $^{\bullet}OH$ to form monohydroxylation (B) or dihydroxylation (C). The carbon atom in the isopropyl group undergoes oxidation by $^{\bullet}OH$, subsequently forming (F) and (D). These compounds are then further oxidized by ROS, such as $^{\bullet}O_2^-$ and $^1O_2$, resulting in the generation of (G) and (E). On the other hand, compound (B) also triggers the production of (H) and (I) *via* $^{\bullet}O_2^-$ induced dehydroxylation, followed by ring-opening reactions yielding (E). **Pathway II:** the cleavage of the isopropyl C–C bond *via* β-scission was confirmed through the

observation of (J) and (K). This process is caused by the attack of oxidation-active photogenerated h^+, which are subsequently oxidized to species (L) and (M). Following the ring-opening reaction of the benzene ring, (M) was further converted into (N). Finally, (E) and (N) were oxidized and mineralized, leading to the formation of small molecules such as organic acids, CO_2, and water.

Conclusions

In conclusion, three highly crystalline vinylene-linked COFs based on the electron-deficient triazine unit were successfully prepared. The TMT-TT-COF and TMT-N-COF exhibit a stronger donor–acceptor (D–A) structure, which enhances the intralayer charge transfer in contrast to the TMT-BT-COF. More particularly, TMT-TT-COF is assembled involving S-containing thiophene moieties, exhibiting a narrower bandgap, more robust intramolecular charge carrier transport and alleviated recombination, ultimately leading to greatly enhanced photocatalytic performance. Meanwhile, this investigation offers valuable insights into the strategic design of COFs aimed at enhancing H_2O_2 synthesis and fostering the generation of abundant ROS, consequently facilitating the effective degradation of BPA. This achievement is realized through the deliberate integration of donor and acceptor functional groups within the COF skeletons. Furthermore, it also contributes to the potential utilization of H_2O_2 generated by COFs, thereby establishing a pathway for tangible applications in diverse practical applications.

Author contributions

Maojun Deng conceived the idea, designed the experiments and wrote the original draft. Linyang Wang performed the data analysis, writing and editing draft, Zhongliang Wen, Jeet Chakraborty, Jiamin Sun and Guizhen Wang were involved in the validation, investigation and resources. Pascal Van Der Voort supervised the project and provided funding acquisition, data analysis, and manuscript revision. All authors contributed to discussions and finalizing the manuscript.

Conflicts of interest

There are no conflicts to declare.

Acknowledgements

We thank Prof. Dirk Poelman (UGent) for helping with the Solid-state UV-vis measurements. We also would like to thank Chunhui Liu and Zhiwang Cai for testing PL. M. J. D. (202107565003), L. Y. W (202108110055), Z. L. W. (202207565006), and J. M. S. (201906060159) acknowledge the financial support from the China Scholarship Council (CSC). J. C. acknowledge financial support from UGent (BOF. PDO. 2022.0032.01). PVDV acknowledges the Flemish Research Foundation (FWO Vlaanderen) for financial support *via* project G020521N, J. M. S. acknowledges the financial support from Ghent University (BOF CSC preference program 01SC0619).

References

1 Y. Zhang, H. Ma, X. Chen, W. Wang, F. Li, T. Qiang, Y. Shen and Y. Cong, *J. Hazard. Mater.*, 2023, **443**, 130250.
2 W.-D. Oh, L.-W. Lok, A. Veksha, A. Giannis and T.-T. Lim, *Chem. Eng. J.*, 2018, **333**, 739–749.
3 F. Farzin, M. K. Rofouei, M. Mousavi and J. B. Ghasemi, *J. Phys. Chem. Solids*, 2022, **163**, 110588.
4 J. M. Campos-Martin, G. Blanco-Brieva and J. L. G. Fierro, *Angew. Chem., Int. Ed.*, 2006, **45**, 6962–6984.
5 V. R. Choudhary, A. G. Gaikwad and S. D. Sansare, *Angew. Chem.*, 2001, **113**, 1826–1829.
6 C. Xia, Y. Xia, P. Zhu, L. Fan and H. Wang, *Science*, 2019, **366**, 226–231.
7 X. Zeng, Y. Liu, X. Hu and X. Zhang, *Green Chem.*, 2021, **23**, 1466–1494.
8 L. Wang, J. Zhang, Y. Zhang, H. Yu, Y. Qu and J. Yu, *Small*, 2022, **18**, 2104561.
9 X. Li, Z. Le, X. Chen, Z. Li, W. Wang, X. Liu, A. Wu, P. Xu and D. Zhang, *Appl. Catal., B*, 2018, **236**, 501–508.
10 M. Deng, X. Cao, L. Guo, H. Cao, Z. Wen, C. Mao, K. Zuo, X. Chen, X. Yu and W. Yuan, *Dalton Trans.*, 2020, **49**, 2308–2316.
11 M. Sun, Y. Wang, Y. Shao, Y. He, Q. Zeng, H. Liang, T. Yan and B. Du, *J. Colloid Interface Sci.*, 2017, **501**, 123–132.
12 Z. Chen, D. Yao, C. Chu and S. Mao, *Chem. Eng. J.*, 2023, **451**, 138489.
13 L. Yang, Y. Wang, J. Yuan, G. Wang, Q. Cao, H. Fei, M. Li, J. Shao, H. Li and J. Lu, *Chem. Eng. J.*, 2022, **446**, 137095.
14 Y. Ding, S. Maitra, S. Halder, C. Wang, R. Zheng, T. Barakat, S. Roy, L.-H. Chen and B.-L. Su, *Matter*, 2022, **5**, 2119–2167.
15 J. Sun, J. Chakraborty, M. Deng, A. Laemont, X. Feng, Y.-Y. Liu and P. Van Der Voort, *J. Mater. Chem. A*, 2023, **11**, 21516–21540.
16 A. P. Côté, A. I. Benin, N. W. Ockwig, M. O'Keeffe, A. J. Matzger and O. M. Yaghi, *Science*, 2005, **310**, 1166–1170.
17 H. Li, L. Wang and G. Yu, *Nano Today*, 2021, **40**, 101247.
18 M. Deng, J. Sun, A. Laemont, C. Liu, L. Wang, L. Bourda, J. Chakraborty, K. Van Hecke, R. Morent, N. De Geyter, K. Leus, H. Chen and P. Van Der Voort, *Green Chem.*, 2023, **25**, 3069–3076.
19 J. Zhao, J. Ren, G. Zhang, Z. Zhao, S. Liu, W. Zhang and L. Chen, *Chem. – Eur. J.*, 2021, **27**, 10781–10797.
20 W. Li, X. Huang, T. Zeng, Y. A. Liu, W. Hu, H. Yang, Y.-B. Zhang and K. Wen, *Angew. Chem., Int. Ed.*, 2021, **60**, 1869–1874.
21 G. Li, W. Tian, C. Zhong, Y. Yang and Z. Lin, *ACS Appl. Mater. Interfaces*, 2022, **14**, 21750–21757.

22 J. Yang, S. Ghosh, J. Roeser, A. Acharjya, C. Penschke, Y. Tsutsui, J. Rabeah, T. Wang, S. Y. Djoko Tameu, M.-Y. Ye, J. Grüneberg, S. Li, C. Li, R. Schomäcker, R. Van De Krol, S. Seki, P. Saalfrank and A. Thomas, *Nat. Commun.*, 2022, **13**, 6317.
23 Z. Li, T. Deng, S. Ma, Z. Zhang, G. Wu, J. Wang, Q. Li, H. Xia, S.-W. Yang and X. Liu, *J. Am. Chem. Soc.*, 2023, **145**, 8364–8374.
24 Y. Xia, W. Zhang, S. Yang, L. Wang and G. Yu, *Adv. Mater.*, 2023, 2301190, DOI: **10.1002/adma.202301190**.
25 L. Zhai, Z. Xie, C.-X. Cui, X. Yang, Q. Xu, X. Ke, M. Liu, L.-B. Qu, X. Chen and L. Mi, *Chem. Mater.*, 2022, **34**, 5232–5240.
26 J. Sun, H. Sekhar Jena, C. Krishnaraj, K. Singh Rawat, S. Abednatanzi, J. Chakraborty, A. Laemont, W. Liu, H. Chen, Y. Y. Liu, K. Leus, H. Vrielinck, V. Van Speybroeck and P. Van Der Voort, *Angew. Chem., Int. Ed.*, 2023, **62**, e202216719.
27 Y. Mou, X. Wu, C. Qin, J. Chen, Y. Zhao, L. Jiang, C. Zhang, X. Yuan, E. Huixiang Ang and H. Wang, *Angew. Chem., Int. Ed.*, 2023, **62**, e202309480.
28 J.-Y. Yue, L.-P. Song, Y.-F. Fan, Z.-X. Pan, P. Yang, Y. Ma, Q. Xu and B. Tang, *Angew. Chem., Int. Ed.*, 2023, **62**, e202309624.
29 F. Liu, P. Zhou, Y. Hou, H. Tan, Y. Liang, J. Liang, Q. Zhang, S. Guo, M. Tong and J. Ni, *Nat. Commun.*, 2023, **14**, 4344.
30 D. Chen, W. Chen, Y. Wu, L. Wang, X. Wu, H. Xu and L. J. A. C. Chen, *Angew. Chem.*, 2023, **135**, e202217479.
31 X. Xu, Y. Sui, W. Chen, W. Huang, X. Li, Y. Li, D. Liu, S. Gao, W. Wu, C. Pan, H. Zhong, H.-R. Wen and M. Wen, *Appl. Catal., B*, 2024, **341**, 123271.
32 S.-p. Qi, R.-t. Guo, Z.-x. Bi, Z.-r. Zhang, C.-f. Li and W.-g. Pan, *Small*, 2023, 2303632, DOI: **10.1002/smll.202303632**.
33 A. Torres-Pinto, M. J. Sampaio, C. G. Silva, J. L. Faria and A. M. T. Silva, *Appl. Catal., B*, 2019, **252**, 128–137.
34 S. Wei, F. Zhang, W. Zhang, P. Qiang, K. Yu, X. Fu, D. Wu, S. Bi and F. Zhang, *J. Am. Chem. Soc.*, 2019, **141**, 14272–14279.
35 J.-N. Chang, Q. Li, J.-W. Shi, M. Zhang, L. Zhang, S. Li, Y. Chen, S.-L. Li and Y.-Q. Lan, *Angew. Chem., Int. Ed.*, 2023, **62**, e202218868.
36 T. Zeng, S. Jin, S. Li, J. Bao, Z. Jin, D. Wang, F. Dong, H. Zhang and S. Song, *Environ. Sci. Technol.*, 2022, **56**, 9474–9485.
37 L. Wang, J. Sun, M. Deng, C. Liu, S. Ataberk Cayan, K. Molkens, P. Geiregat, R. Morent, N. De Geyter, J. Chakraborty and P. Van Der Voort, *Catal. Sci. Technol.*, 2023, **13**, 6463–6471.
38 X. Yu, B. Viengkeo, Q. He, X. Zhao, Q. Huang, P. Li, W. Huang and Y. Li, *Adv. Sustainable Syst.*, 2021, **5**, 2100184.
39 C. Wu, Z. Teng, C. Yang, F. Chen, H. B. Yang, L. Wang, H. Xu, B. Liu, G. Zheng and Q. Han, *Adv. Mater.*, 2022, **34**, 2110266.
40 H. Ming, D. Wei, Y. Yang, B. Chen, C. Yang, J. Zhang and Y. Hou, *Chem. Eng. J.*, 2021, **424**, 130296.
41 Y. M. Hunge, A. A. Yadav, S. Khan, K. Takagi, N. Suzuki, K. Teshima, C. Terashima and A. Fujishima, *J. Colloid Interface Sci.*, 2021, **582**, 1058–1066.
42 E. B. Simsek, *Appl. Catal., B*, 2017, **200**, 309–322.
43 T. Shi, H. Wang, L. Li, Z. Zhao, C. Wang, X. Zhang and Y. Xie, *Matter*, 2022, **5**, 1004–1015.
44 J. Yang, A. Acharjya, M.-Y. Ye, J. Rabeah, S. Li, Z. Kochovski, S. Youk, J. Roeser, J. Grüneberg, C. Penschke, M. Schwarze, T. Wang, Y. Lu, R. van de Krol, M. Oschatz, R. Schomäcker, P. Saalfrank and A. Thomas, *Angew. Chem., Int. Ed.*, 2021, **60**, 19797–19803.
45 Q. Shang, Y. Liu, J. Ai, Y. Yan, X. Yang, D. Wang and G. Liao, *J. Mater. Chem. A*, 2023, **11**, 21109–21122.